









# The Sleeping Monster: *NuSTAR* Observations of SGR 1806–20, 11 Years After the Giant Flare

George Younes<sup>1,2</sup> , Matthew G. Baring<sup>3</sup>, Chryssa Kouveliotou<sup>1,2</sup> , Alice Harding<sup>4</sup> , Sophia Donovan<sup>1,2</sup>, Ersin Göğüş<sup>5</sup> ,  
Victoria Kaspi<sup>6</sup> , and Jonathan Granot<sup>7</sup> 

<sup>1</sup> Department of Physics, The George Washington University, Washington, DC 20052, USA; [gyounes@gwu.edu](mailto:gyounes@gwu.edu)

<sup>2</sup> Astronomy, Physics and Statistics Institute of Sciences (APSYS), The George Washington University, Washington, DC 20052, USA

<sup>3</sup> Department of Physics and Astronomy, Rice University, MS-108, P.O. Box 1892, Houston, TX 77251, USA

<sup>4</sup> Astrophysics Science Division, NASA Goddard Space Flight Center, Greenbelt, MD 20771, USA

<sup>5</sup> Sabanci University, Orhanlı-Tuzla, İstanbul 34956, Turkey

<sup>6</sup> Department of Physics, McGill University, Montreal, Quebec, H3A 2T8, Canada

<sup>7</sup> Department of Natural Sciences, The Open University of Israel, 1 University Road, P.O. Box 808, Raánana 43537, Israel

Received 2017 October 15; revised 2017 October 25; accepted 2017 October 27; published 2017 December 6

## Abstract

We report the analysis of five *Nuclear Spectroscopic Telescope Array* (*NuSTAR*) observations of SGR 1806–20 spread over a year from 2015 April to 2016 April, more than 11 years following its giant flare (GF) of 2004. The source spin frequency during the *NuSTAR* observations follows a linear trend with a frequency derivative  $\dot{\nu} = (-1.25 \pm 0.03) \times 10^{-12} \text{ Hz s}^{-1}$ , implying a surface dipole equatorial magnetic field  $B \approx 7.7 \times 10^{14} \text{ G}$ . Thus, SGR 1806–20 has finally returned to its historical minimum torque level measured between 1993 and 1998. The source showed strong timing noise for at least 12 years starting in 2000, with  $\dot{\nu}$  increasing one order of magnitude between 2005 and 2011, following its 2004 major bursting episode and GF. SGR 1806–20 has not shown strong transient activity since 2009, and we do not find short bursts in the *NuSTAR* data. The pulse profile is complex with a pulsed fraction of  $\sim 8\%$  with no indication of energy dependence. The *NuSTAR* spectra are well fit with an absorbed blackbody,  $kT = 0.62 \pm 0.06 \text{ keV}$ , plus a power law,  $\Gamma = 1.33 \pm 0.03$ . We find no evidence for variability among the five observations, indicating that SGR 1806–20 has reached a persistent and potentially its quiescent X-ray flux level after its 2004 major bursting episode. Extrapolating the *NuSTAR* model to lower energies, we find that the 0.5–10 keV flux decay follows an exponential form with a characteristic timescale  $\tau = 543 \pm 75 \text{ days}$ . Interestingly, the *NuSTAR* flux in this energy range is a factor of  $\sim 2$  weaker than the long-term average measured between 1993 and 2003, a behavior also exhibited in SGR 1900+14. We discuss our findings in the context of the magnetar model.

**Key words:** stars: individual (SGR 1806–20) – stars: magnetars – stars: neutron – X-rays: stars

## 1. Introduction

Magnetars are a small class of isolated neutron stars believed to be powered by the decay of their strong ( $B \sim 10^{14-16} \text{ G}$ ) internal magnetic fields (see Mereghetti 2008; Turolla et al. 2015; Kaspi & Beloborodov 2017, for reviews). This characteristic induces very peculiar observational properties to the class. Almost all magnetars have been observed to enter bursting episodes where they emit 10 s to 100 s of short ( $\sim 0.1 \text{ s}$ ), bright ( $10^{37-41} \text{ erg}$ ), hard X-ray bursts within the span of days to weeks (e.g., Israel et al. 2008; Lin et al. 2011; van der Horst et al. 2012; Göğüş et al. 2017). These episodes are usually accompanied by changes in the spectral and temporal properties of the source persistent X-ray emission. The persistent X-ray flux increases, occasionally by as many as three orders of magnitude (e.g., Rea & Esposito 2011; Kargaltsev et al. 2012; Scholz et al. 2012), and their spectra harden. The shape of the pulse profile and the fraction of the pulsed flux change, while the source timing properties vary either in the form of a glitch or as a more gradual change in the spindown rate (e.g., Dib & Kaspi 2014; Archibald et al. 2015). The source properties recover to pre-outburst levels months to years later. Hence, observations of magnetar outbursts are a key ingredient to understanding the physics behind these perplexing sources and the geometrical locale of their activity.

SGR 1806–20 is historically the most active magnetar in the family, known to emit short bursts regularly since its discovery. Major bursting episodes have been recorded several times, with

the strongest one occurring from mid to late 2004. This episode culminated with the emission of the strongest giant flare (GF) on record so far (Hurley et al. 2005; Gaensler et al. 2005), 2004 December 27 (MJD 53366). Radical changes in the source temporal and spectral properties have been observed since 1995, with its X-ray spectral shape hardening gradually and its frequency derivative increasing monotonically up to 2002 (Mereghetti et al. 2005; Woods et al. 2007). Around the time of the 2004 bursting episode and the GF, erratic changes to the timing properties of the source were observed (Woods et al. 2007). The 0.5–10 keV persistent flux from the source started increasing shortly before the major bursting episode of 2004, reaching a maximum around its peak activity. The GF did not have a measurable effect on the spectral properties of the source persistent emission, while it did decrease the pulsed fraction (PF) from its historical level of 8% to about 3% (Rea et al. 2005; Tiengo et al. 2005).

In Younes et al. (2015b, Y15 hereafter), we studied the X-ray properties of SGR 1806–20 up to mid 2011, over seven years following the GF. We found that the torque on the star still showed strong variation and, on average, remained at a historically high level, an order of magnitude larger than the one measured between 1994 and 1998. The pulse profile was double peaked with a modest contribution from a second harmonic. The source flux started decreasing in 2005 toward its quiescent value, while at the same time its blackbody (BB) temperature  $kT$  cooled and its power law (PL) slightly softened

**Table 1**  
*NuSTAR* Observations and Source Timing Properties

Observation ID	Date	Exposure (ks)	$\nu$ (error) (Hz)	PF (error) (%)
30102038002 <sup>a</sup>	2015 Apr 17	33.2	...	<15
30102038004	2015 Jun 29	28.7	0.129030(3)	9(2)
30102038006	2015 Aug 19	31.2	0.129023(2)	7(1)
30102038007	2015 Nov 11	45.7	0.129013(2)	8(2)
30102038009	2016 Apr 12	29.9	0.128994(4)	7(1)

**Note.**

<sup>a</sup> No pulse frequency measurement was possible due to strong contamination from stray light. Pulse fraction upper limit is consistent with the rest of the measurements.

(Y15). Here, we report on the analysis of five *Nuclear Spectroscopic Telescope Array (NuSTAR)* observations of SGR 1806–20, spanning a full year from 2015 April to 2016 April, over 11 years following its major bursting episode and GF. We present the observations and data reduction in Section 2, and the data analysis and results are presented in Section 3. Finally, both the temporal and spectra results are discussed in Section 4 in the context of the magnetar paradigm, focusing on field structure and magnetospheric emission models.

## 2. Observations and Data Reduction

The *NuSTAR* (Harrison et al. 2013) consists of two identical modules FPMA and FPMB operating in the energy range 3–79 keV. *NuSTAR* observed SGR 1806–20 on five occasions, the first of which took place on 2015 April 17. The last observation was taken on 2016 April 12 (Table 1). We processed the data using the *NuSTAR* Data Analysis Software, *nustardas* version v1.5.1. We analyzed the data using the *nuproducts* task (which allows for spectral extraction and generation of ancillary and response files) and *HEASOFT* version 6.19. We extracted source events around the source position using a circular region with 45'' radius, which maximized the signal-to-noise ratio (S/N). Background events were extracted from an annulus around the source position with inner and outer radii of 80'' and 120'', respectively. Only in the first observation did we have both modules strongly contaminated by stray light, whereas at most, one module showed stray light contamination in the following four observations.

We also include in our analysis one *Chandra* observation taken on 2000 August 15, with a total exposure of 31 ks (obs. ID 746). The source was placed on the ACIS S3 chip, which is used in a 1/4 subarray mode, reducing the readout time to 0.8 s. The spectral analysis of this observation was never reported in the literature to our best of knowledge, due to mild pile-up issues with a fraction of ~8% of total counts being piled-up (Kaplan et al. 2002). To identify the historical flux level from SGR 1806–20, here we perform spectral analysis of this observation. CIAO version 4.9 was employed for our data reduction purposes. We extract source counts from a circle with radius of 2'' centered on the best location from the source (Kaplan et al. 2002). Background counts are extracted from an annulus region with inner and outer radii of 10'' and 20'', respectively, centered on the same location as the source circular region. The ancillary and response files were created using the *mkacisrmf* and *mkarf* tools, respectively. Two methods were adopted to mitigate the pile-up problem in the

observation. Because the pile-up fraction is relatively low, we added the *Chandra* pile-up model (included in XSPEC, Davis 2001) to the full spectral model we use to fit the source spectrum (Section 3.2). As a validation of this method, the source spectrum was extracted from the pile-up free wings of the ACIS psf, excluding the piled-up 1''2 central core. We find consistent results between both methods. In Section 3.2, we only report the spectral results as derived using the full PSF while including the pile-up model in the fit.

The spectral analysis of the *NuSTAR* and *Chandra* data was performed using XSPEC version 12.9.0k (Arnaud 1996). The photoelectric cross sections of Verner et al. (1996) and the abundances of Wilms et al. (2000) are used throughout to account for absorption by neutral gas. We bin the spectra to have a minimum of five counts per bin, and use the Cash statistic (C-stat) in XSPEC for model parameter estimation and error calculation. We used the *goodness* command for goodness-of-fit estimation. We double-checked our spectral analysis results by binning the spectra to have a S/N of seven (about 50 counts per bin) and using the typical  $\chi^2$  method. Both methods gave consistent results. For all spectral fits, we added a multiplicative constant normalization between FPMA and FPMB, frozen to 1 for the former and allowed to vary for the latter to account for any calibration uncertainties between the two instruments. We find that this uncertainty clusters around ~5%. Finally, all quoted errors are at the  $1\sigma$  level unless otherwise noted.

## 3. Results

### 3.1. Timing Analysis

To maximize the S/N for our timing analysis, we considered only source events in the energy range 3–50 keV. We corrected these events' arrival times to the solar barycenter and to drifts in the *NuSTAR* clock caused by temperature variations (Harrison et al. 2013). We applied the  $Z_{m=2}^2$  algorithm to search for the pulsations from the source. We chose  $m = 2$ , given that the 2011 *XMM-Newton* observations of the source still showed a double-peaked profile with modest contribution from the second harmonic (Y15). We searched the interval 0.126–0.130 Hz with a size step of  $2.0 \times 10^{-5}$  Hz, which encapsulates the expected frequencies for the different frequency derivatives that SGR 1806–20 has shown since 1993. In all but the first observation, we detect a signal at around  $8\sigma$  (trial corrected). The results are given in Table 1 and shown in Figure 1. The frequencies follow a linear trend with a frequency derivative  $\dot{\nu} = (-1.25 \pm 0.03) \times 10^{-12}$  Hz s<sup>-1</sup>.

We folded the event files of each of the last four observations in the energy range 3–50 keV at their respective periods found above, creating a pulse profile (PP), which we then background corrected (Figure 2). These PPs looked similar to the ones following the 2004 GF, i.e., complex with a multi-peak structure (e.g., Mereghetti et al. 2005; Woods et al. 2007, Y15). Therefore, we fit these PPs with a Fourier series including the contribution from two harmonics (e.g., Bildsten et al. 1997; Younes et al. 2015a, Figure 2). The fits are good resulting in a  $\chi^2$  of ~5 for 7 degrees of freedom (d.o.f.).

We estimated the rms PF for these observations in the energy range 3–50 keV. We find that the PF is stable at around 8%. We also derive a  $3\sigma$  upper limit of 15% on the PF of a fiducial signal for observation 1. These PFs level are consistent with the historical level as measured with *ASCA* and

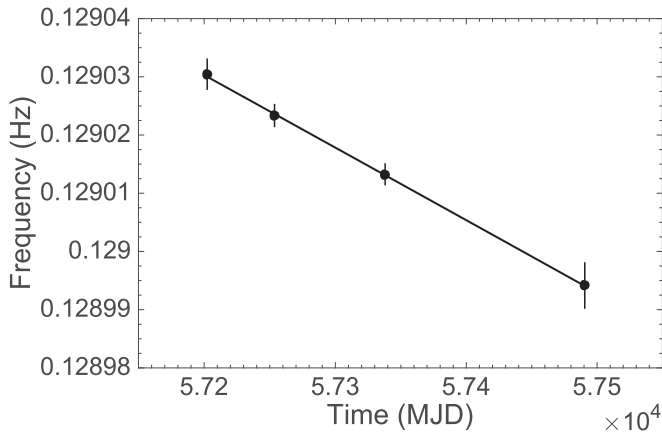


**Figure 1.** Frequency (black dots) and best-fit linear trend (solid line) to the four *NuSTAR* observations where the signal was detected. The slope of the best fit, hence frequency derivative, is  $\dot{\nu} = (-1.25 \pm 0.03) \times 10^{-12} \text{ Hz s}^{-1}$ .

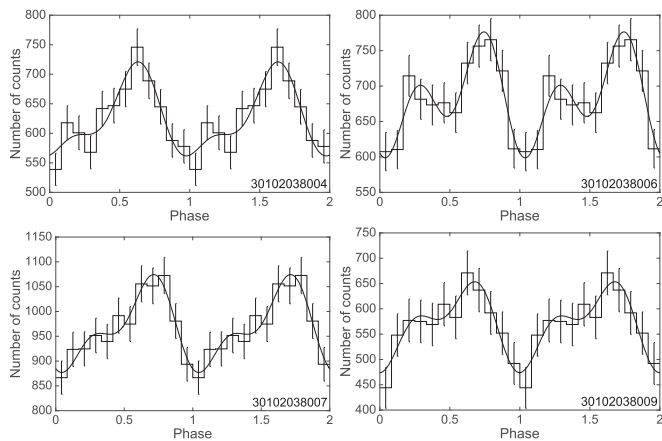


**Figure 2.** *NuSTAR* 3–50 keV background-corrected pulse profiles of SGR 1806–20 where the pulse was detected, i.e., for the last four observing runs listed in Table 1. Two cycles are shown for clarity. The solid line is the best-fit Fourier series including the contribution from two harmonics.

*BeppoSAX* around 1995. The only change in PF for SGR 1806–20 was observed immediately after the GF when it dropped to a minimum of 3% (Rea et al. 2005; Tiengo et al. 2005). We searched for any changes in pulse morphology and/or PF with energy by considering events above and below 10 keV separately. We find no dependence, within error, in these two properties within the energy range considered.

We extended the work of Woods et al. (2007) and Y15 to build the most comprehensive view of the torque evolution of SGR 1806–20 from 1993 to 2016. The middle panel of Figure 3 shows the timing history of SGR 1806–20 up to the last *NuSTAR* observation in 2016 April, over 11 years after the GF. The blue dots are data from Woods et al. (2007), the red dots are *XMM-Newton* data from Y15, while the black dots are the frequencies as derived with *NuSTAR*. The lines represent average frequency derivative over periods of relatively stable spin. The bottom panel shows the instantaneous frequency derivative calculated between two adjacent frequency data points (the blue triangles are data taken from Woods et al. (2007), the red triangles from Y15, and the black triangles are for *NuSTAR*). Both the instantaneous and the average frequency derivatives as derived with *NuSTAR* data show that the source has returned to a level consistent with its historical level, e.g.,  $\dot{\nu} = (-1.22 \pm 0.17) \times 10^{-12} \text{ Hz s}^{-1}$  between 1996

November 5 and 18 (Woods et al. 2000). Assuming a similarly abrupt change in the frequency trend as seen with the other two changes, the extrapolation of the *NuSTAR* frequency points (solid line) indicates that this change may have likely started around mid 2012.

Similar to the previous works, we also report on the burst history from the source from 2011 to end of 2016 (Figure 3, top panel). These are bursts reported in the Gamma-ray Coordinates Network (GNC) and mainly seen with wide field-of-view instruments within the InterPlanetary Network (IPN). It is evident that the source has been in a quiet state with no major bursting episode since about 2009. Finally, we note that we searched all *NuSTAR* data for short bursts using the method of Gavriil et al. (2004) in the energy range 3–79 keV. We used multiple time bins (16, 32, 64, 128, and 256 ms); we found no evidence of low-level bursting activity in SGR 1806–20. All of the above results are discussed below in Section 4.

### 3.2. Spectral Analysis

We fit all *NuSTAR* spectra simultaneously with an absorbed PL and BB model. We link the absorption between the five observations while we keep all other parameters free to vary. We find a good fit with a C-stat of 5505 for 5347 d.o.f. (goodness  $\approx 62\%$ ). We find an absorption column density  $N_{\text{H}} = (1.0 \pm 0.3) \times 10^{23} \text{ cm}^{-2}$ , consistent with *XMM-Newton* spectral results (Y15). The rest of the parameters, i.e., the BB temperature, the PL photon index, and their respective fluxes, are consistent between all observations within errors (Table 2). Hence, to obtain a representative average between the observing runs, we refit all spectra, simultaneously linking all parameters between the spectra. We find an equally good fit with a C-stat of 5551 for 5369 degrees of freedom d.o.f (goodness  $\approx 59\%$ ). This result indicates that the persistent X-ray emission of source is currently in a steady state.

We find a PL photon index  $\Gamma = 1.33 \pm 0.03$ , a BB temperature  $kT = 0.62 \pm 0.06 \text{ keV}$ , and, assuming a spherical surface for the thermally emitting BB region, a radius  $R = 1.5 \pm 0.4 \text{ km}$  (Table 2). For an orthogonal rotator, a surface hot spot with this radius would clearly evince a higher pulse fraction than is presented in Figure 2; more aligned magnetic and spin axes reduce the expected pulse fraction accordingly. The 3–79 keV flux is  $(3.07 \pm 0.04) \times 10^{-11} \text{ erg s}^{-1} \text{ cm}^{-2}$ . Extending the *NuSTAR* model down to 0.5 keV, we estimate a 0.5–79 keV flux of  $(3.68 \pm 0.05) \times 10^{-11} \text{ erg s}^{-1} \text{ cm}^{-2}$  and a luminosity  $(3.33 \pm 0.06) \times 10^{35} \text{ erg s}^{-1}$ , assuming a distance of 8.7 kpc (Bibby et al. 2008). In this energy range, we find a BB flux  $F_{\text{BB}} = (4.8 \pm 1.7) \times 10^{-12} \text{ erg s}^{-1} \text{ cm}^{-2}$  and a PL flux  $F_{\text{PL}} = (3.21 \pm 0.04) \times 10^{-11} \text{ erg s}^{-1} \text{ cm}^{-2}$  implying a ratio  $F_{\text{PL}}/F_{\text{BB}} \approx 7$  (we note the weak constraint on the BB flux due to the lack of *NuSTAR* sensitivity at energies below 3 keV).

We fit the *Chandra* spectrum with the same model as the *NuSTAR* data of a BB+PL (including the XSPEC pile-up model; see Section 2). We find a good fit with a C-stat of 498 for 512 degrees of freedom d.o.f. (goodness  $\approx 43\%$ ). The best-fit parameters are summarized in Table 2. We find a total 0.5–10 keV flux of  $2.3_{-0.4}^{+0.3} \times 10^{-11} \text{ erg s}^{-1} \text{ cm}^{-2}$ .

Figure 5 shows the evolution of the total, absorption-corrected 0.5–10 keV flux of SGR 1806–20 from 2000 up to the last *NuSTAR* observation. We also include the source average flux measured from 1993 to 2001 with *ASCA* and *BeppoSAX* (horizontal solid line, Woods et al. 2007). The enhancement of quiescent emission above its long-term

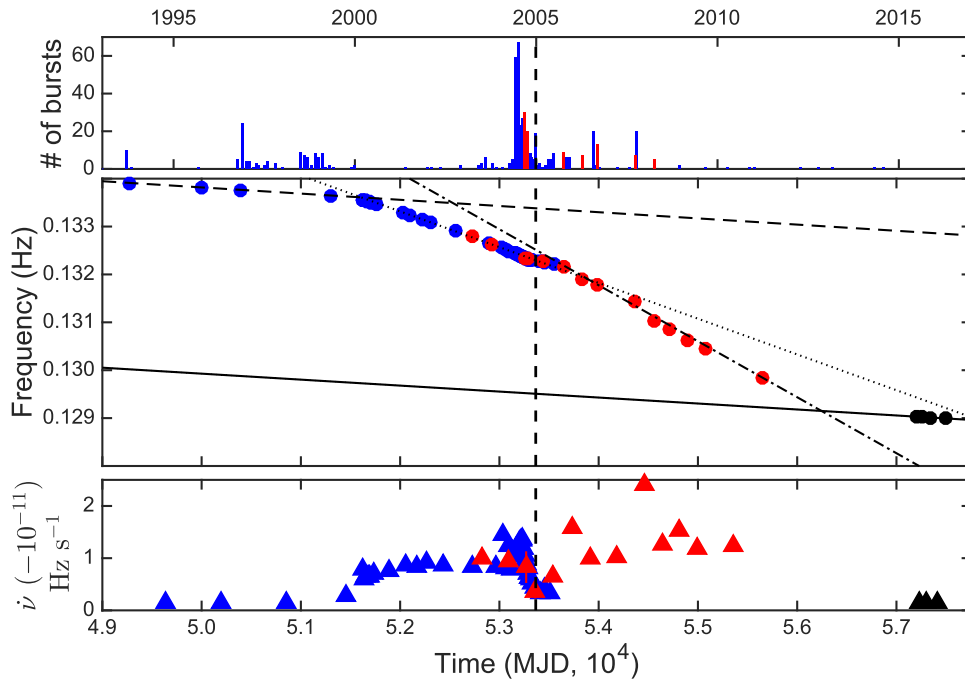


**Figure 3.** Extension of Woods et al. (2007) and Younes et al. (2015b, Y15) showing the frequency and frequency derivative history of SGR 1806–20 from mid 1993 until 2016 April. Top panel: number of bursts (per 30 days). Data for the blue bars are collected from Woods et al. (2007), Y15, including bursts reported in GCNs from 2012 to 2016. Red bars represent bursts as detected by *XMM-Newton* (Y15). The dashed vertical line marks 2004 December 27, the date of the giant flare. Middle panel: spin frequency history. Blue dots are adopted from Woods et al. (2007), representing data from five different X-ray telescopes, the red dots are from Y15, while the black dots are the *NuSTAR* frequency measurements. The vertical dashed line in all three panels denotes the time of the GF. The dashed and dotted lines are fits to the frequency derivative from 1993 to 2000 January ( $\dot{\nu} = -1.48 \times 10^{-12}$  Hz s $^{-1}$ ), and 2001 January to 2004 April ( $\dot{\nu} = -8.69 \times 10^{-12}$  Hz s $^{-1}$ ; Woods et al. 2007). The dotted-dashed line is the fit to frequency measurements from 2005 July up to 2011 April ( $\dot{\nu} = -1.35 \times 10^{-11}$  Hz s $^{-1}$ ; Y15). The black solid line is the best-fit linear trend to the *NuSTAR* data ( $\dot{\nu} = -1.25 \times 10^{-12}$  Hz s $^{-1}$ ). Bottom panel: instantaneous frequency derivative between two consecutive frequency measurements. Note the return of the instantaneous frequency derivatives at the time of the *NuSTAR* observations to the 1995 historical level. See the text for more details.

persistent level reached its peak around the *XMM-Newton* observation of 2004 September 6 (observation ID 0205350101, Woods et al. 2007, Y15). We fit the flux evolution starting at this data point with an exponential decay function of the form  $F(t) = Ke^{-(t-t_0)/\tau} + F_{\text{per}}$ . Here,  $K$  is normalization,  $t_0$  is the time of the above *XMM-Newton* observation,  $\tau$  is the mean lifetime for which the normalization decays by 63%, and  $F_{\text{per}}$  is the constant persistent flux level assumed to be the one measured with *NuSTAR*. We find a good fit with a reduced  $\chi^2$  of 1.2 for 15 d.o.f., with  $\tau = 543 \pm 75$  days and  $K = (3.2 \pm 0.4) \times 10^{-11}$  erg s $^{-1}$  cm $^{-2}$ . The time for which the normalization decays by 95%, i.e., the flux has decayed back to 5% of its persistent level, is  $1629 \pm 225$  days. The total energy emitted in the outburst during this time interval is  $E = (1.4 \pm 0.4) \times 10^{43}$  erg.

The striking observational result in Figure 5 is the noticeable difference in the total 0.5–10 keV flux in the recent *NuSTAR* flux compared with the pre-outburst long-term average, which persisted from 1993 to 2003. The ratio of the 0.5–10 keV *NuSTAR* flux to the historical average flux is  $0.53 \pm 0.10$ . The *NuSTAR* fluxes derived for each model component as compared with those of *Chandra* (Table 2) imply that the PL component has decreased beyond its flux measured pre-outburst. On the other hand, the high uncertainty on the BB flux measurement prevents us from drawing firm conclusions on whether the BB component is behaving similarly to the PL one. Nevertheless, combining our results with all the values reported in the literature (Woods et al. 2007; Y15) we find that neither the BB temperature nor the PL index show any clear

trend in evolving from historical pre-outburst values to those determined during the recent quiescent epoch.

## 4. Summary and Discussion

### 4.1. Timing Evolution

Our *NuSTAR* observations spread over a year from 2015 April to 2016 April reveal the return of SGR 1806–20 spin derivative,  $\dot{\nu} = (-1.25 \pm 0.03) \times 10^{-12}$  Hz s $^{-1}$ , to its historical minimum level derived more than 16 years earlier, e.g.,  $\dot{\nu} = (-1.22 \pm 0.17) \times 10^{-12}$  Hz s $^{-1}$  between 1996 November 5 and November 18 (Woods et al. 2000). During the time in between, SGR 1806–20 showed radical changes in its temporal properties while also being the most consistently burst-active magnetar. It showed a major bursting episode in 2004 and several moderate ones (10 s of bursts) almost yearly from 1997 until 2009 (Woods et al. 2002; Woods et al. 2007; Mereghetti et al. 2005; Y15). Since 2009, the source has been uncharacteristically quiet, with only a few single bursts detected every year (Figure 3). Hence, this level of torque that we derive with *NuSTAR* can be considered the quiescent state magnetic configuration of SGR 1806–20. Assuming that this corresponds to its dipole magnetic radiation, we estimate a magnetic field strength at the equator  $B = 7.7 \times 10^{14}$  G, close in value to those of SGR 1900+14 (Woods et al. 1999; Mereghetti et al. 2006) and 1E 1841–045 (Dib & Kaspi 2014). We also estimate a spindown age  $\tau = 1.6$  kyr, and note that because the torque evolution over the last 11 years has been so profound, it is clear that such spindown ages are not an excellent proxy for the true stellar age. The last two *XMM-Newton* observations

**Table 2**  
Spectral Parameters for the BB+PL Best-fit Model

Observation ID	$N_{\text{H}}$ ( $10^{22} \text{ cm}^{-2}$ )	$kT$ (keV)	$R^a$ (km)	$\log F_{\text{BB}}$ ( $\text{erg s}^{-1} \text{ cm}^{-2}$ )	$\Gamma$	$\log F_{\text{PL}}$ ( $\text{erg s}^{-1} \text{ cm}^{-2}$ )	$\log F_{\text{tot}}$ ( $\text{erg s}^{-1} \text{ cm}^{-2}$ )
<i>NuSTAR</i> Observations, Parameters Free to Vary							
30102038002	$10.0 \pm 3.0$	$0.67^{+0.10}_{-0.09}$	$1.1^{+0.7}_{-0.4}$	$-11.63^{+0.16}_{-0.18}$	$1.36 \pm 0.05$	$-10.50 \pm 0.01$	$-10.47 \pm 0.01$
30102038004	(L)	$0.59^{+0.09}_{-0.07}$	$1.6^{+1.0}_{-0.6}$	$-11.65^{+0.18}_{-0.19}$	$1.38 \pm 0.04$	$-10.53 \pm 0.01$	$-10.50 \pm 0.01$
30102038006	(L)	$0.59^{+0.07}_{-0.06}$	$1.8^{+0.9}_{-0.7}$	$-11.54^{+0.15}_{-0.16}$	$1.27 \pm 0.04$	$-10.48 \pm 0.01$	$-10.45 \pm 0.01$
30102038007	(L)	$0.61^{+0.08}_{-0.06}$	$1.7^{+1.0}_{-0.6}$	$-11.50 \pm 0.15$	$1.34^{+0.04}_{-0.05}$	$-10.53 \pm 0.01$	$-10.49 \pm 0.01$
30102038009	(L)	$0.67^{+0.10}_{-0.09}$	$1.2^{+0.8}_{-0.4}$	$-11.54^{+0.14}_{-0.15}$	$1.31 \pm 0.05$	$-10.54 \pm 0.01$	$-10.50 \pm 0.01$
<i>NuSTAR</i> Observations, Parameters Linked between All Observations							
	$10.0 \pm 2.0$	$0.62 \pm 0.06$	$1.5 \pm 0.4$	$-11.57 \pm 0.15$ $-11.32 \pm 0.15^b$	$1.33 \pm 0.03$	$-10.518 \pm 0.006$ $-11.14 \pm 0.04^b$	$-10.497 \pm 0.005$ $-10.92 \pm 0.04^b$
<i>Chandra</i> Observation, 2000 August 15							
743	$10.0 \pm 1.0$	$0.6^{+0.16}_{-0.1}$	$1.9^{+1.1}_{-0.6}$	$-11.14^{+0.2}_{-0.3}$	$1.2^{+0.5}_{-0.3}$	$-10.82 \pm 0.09$	$-10.64^{+0.05}_{-0.08}$

**Notes.**

<sup>a</sup> Derived by adopting an 8.7 kpc distance (Bibby et al. 2008). *NuSTAR* fluxes are derived in the 2–79 keV range, except for those indicated in footnote b.

<sup>b</sup> Fluxes derived in the energy range 0.5–10 keV. *Chandra* fluxes are derived in the 0.5–10 keV. Listed uncertainties are at the  $1\sigma$  level.

indicate that the source was still at a historically high  $\dot{\nu}$  level in 2011. Due to the lack of observations between 2011 and 2015, we cannot exactly track the recovery of the spindown from the source in transitioning from the high  $\dot{\nu}$  state to the perennial one. However, if we conjecture that the return to the minimum level is related to the lack of bursting activity, with the last moderate bursting episode occurring in 2009, we place a lower limit on the recovery timescale of  $\sim 2$  years. This estimate agrees with the projected time of the torque change (mid 2012) mentioned in Section 3.1.

Similar to SGR 1806–20, XTE J1810–197, the first so-called transient magnetar (Ibrahim et al. 2004), is another source in the class to have returned to a historical minimum level after displaying strong timing anomalies following an outburst. A few months after the onset of its 2003 outburst,  $\dot{\nu}$  reached a factor of eight larger than its minimum observed value (Halpern & Gotthelf 2005; Bernardini et al. 2009). Interestingly, the source frequency derivative returned back to its pre-outburst minimum around 2007, four years after the outburst, and remained there until mid 2014 (Camilo et al. 2016; Pintore et al. 2016). 1E 1048.1–5937 also shows variation in  $\dot{\nu}$  following its quasi-periodic outbursts, sometime as large as a factor of 10. The torque then returns to its nominal value on a timescale  $\gtrsim 1$  year (Archibald et al. 2015). On the other hand, SGR J1745–2900, the Galactic center magnetar that went into outburst in 2013 April (Kennea et al. 2013; Mori et al. 2013) has shown an increase of  $\dot{\nu}$  by a factor of 4.5, and no sign of decrease 3.5 years following the outburst (Kaspi et al. 2014; Coti Zelati et al. 2017). Last but not least, SGR 1900+14 has also shown strong timing noise following burst-active episodes, e.g., with  $\dot{\nu}$  increasing by a factor of five following its late 1998 major bursting episode and GF (Woods et al. 2002; Mereghetti et al. 2006). There is no published information on the source  $\dot{\nu}$  following its 2006 major bursting episode, hence, at the current time, its  $\dot{\nu}$  fate remains unknown (G. Younes et al. 2017, in preparation). Due to the scarce data and the low number of sources, it is not yet possible to do a systematic comparison between the different objects. Nonetheless, such enhanced spindown post-outburst is common in

magnetars, even those with different levels of bursting behavior, and with different recovery timescales.

The evolution of the timing signatures over durations spanning a few to 10 years is relevant to the transient powering of magnetar magnetospheres, both prior to and subsequent to bursting activity. The leading model for activation of closed field regions in magnetars considers dynamic, twisted magnetospheres that generate electric fields and currents, a concept proposed by Thompson et al. (2002) for the quiescent emission, and embellished upon by Beloborodov & Thompson (2007). Departures from dipolar field geometry by small twist angles  $\Delta\varphi \ll 1$  are invoked, and these precipitate currents  $j \sim [c\mathbf{B}/(4\pi r)]\Delta\varphi \sin^2\vartheta$  at magnetic colatitude  $\vartheta$  that generate electric field components  $E_{\parallel} \sim \sqrt{4\pi m_e c} |j|/e$  parallel to the local field (see Beloborodov & Thompson 2007 for details). The ensuing acceleration can easily generate a hot corona that persists for long activation times. In Beloborodov & Thompson (2007), the resistive decay timescale for the twist via ohmic dissipation couples both the electric potential, which is universally near the 1 GeV level, and also the X-ray luminosity; thus, those authors conclude that twist dissipation activity in magnetars triggered by bursting activity should last for timescales in the realm of several months to a few years.

While this estimate is fairly close to the  $e$ -folding time for relaxation that is inferred here from our timing results, the precise twist decay timescale determination requires detailed simulational modeling. The recent developments of Parfrey et al. (2013) and Chen & Beloborodov (2017) forge steps in this direction, and, in particular, the particle-in-cell plasma simulations of Chen & Beloborodov (2017) confirm that untwisting of the magnetosphere does arise on ohmic dissipation timescales. Yet, in this theory, the twists define a field morphology perturbation in the inner magnetosphere, and it remains to be determined how and if such structural deformations can account for the large torque changes that must accompany the amplifications of  $\dot{\nu}$  by a factor of 10 overall.

As an alternative origin, we observe that enhanced plasma loading of magnetar winds may contribute significantly to the

torque evolution. The increase in  $\dot{\nu}$  following periods of bursting and the gradual return to a quiescent  $\dot{\nu}$  and flux level in SGR 1806-20 is consistent with the picture outlined by Harding et al. (1999; see also Tong et al. 2013) of magnetar bursts leading to episodic particle wind outflow that temporarily increases the spindown rate, on top of a persistent magnetic dipole spin evolution. From Equation (12) of Harding et al. (1999), assuming that the wind luminosity  $L_p$  is much larger than the dipole spindown power,  $\dot{E}_D$ , then  $L_p \sim (\dot{\nu}_W/\dot{\nu}_D)^2 \dot{E}_D$ , where  $\dot{\nu}_W$  is the enhanced frequency derivative following bursting periods, and  $\dot{\nu}_D$  is the frequency derivative of magnetic dipole spindown. Adopting the historical frequency derivative  $\dot{\nu}_D = -1.22 \times 10^{-12} \text{ Hz s}^{-1}$  that is very close to the present *NuSTAR* result (see the caption of Figure 3) to represent the long-term value for the magnetic dipole torque, and using the increased frequency derivative measured over the two periods,  $\dot{\nu}_W = -8.69 \times 10^{-12} \text{ Hz s}^{-1}$  (for 2001–2004) and  $\dot{\nu}_W = -1.35 \times 10^{-11} \text{ Hz s}^{-1}$  (2005–2011), the estimated wind luminosities producing the enhanced torque are  $L_p \sim 50.7 \dot{E}_D = 1.6 \times 10^{35} \text{ erg s}^{-1}$  (for 2001–2004) and  $L_p \sim 122 \dot{E}_D = 3.8 \times 10^{35} \text{ erg s}^{-1}$  (2005–2011) for the respective epochs.

These  $L_p$  values are similar to the X-ray luminosity estimated in Section 3.2 from the spectral fits of the *NuSTAR* data, indicating that the quiescent luminosity and the enhanced particle wind power implied by the torque changes are both around  $100\dot{E}_D$ . This comparability may be coincidental, though a connection between wind power lost to infinity and luminosity in trapped plasma that is dissipated in radiative form is naturally expected; the detailed nature of this coupling is not yet understood. The increased particle flux following bursting activity can deposit a large amount of energy in the magnetar’s environs. This possibility for transient powering of the newly discovered nebula around magnetar Swift J1834.9-0846 (Younes et al. 2012, 2016) was explored by Granot et al. (2017). It is therefore of significant interest how much particle power active burst episodes associated with GFs contribute to the cumulative, long-term energetics of a surrounding nebula. In particular, how such transient contributions compare with those of less dynamic and more prolonged strong wind epochs coupled with somewhat enhanced  $\dot{\nu}$  values.

#### 4.2. Flux History

The flux from the source has now reached a persistent level of the order of  $1.2 \times 10^{-11} \text{ erg s}^{-1} \text{ cm}^{-2}$  in the 0.5–10 keV range (after extrapolating the *NuSTAR* model to the lower end). The flux decay prior to our observations follows a simple exponential function with a characteristic timescale  $\tau = 543$  days. Such long decay timescales have been seen in other magnetars (e.g., Scholz et al. 2014; Alford & Halpern 2016; Coti Zelati et al. 2017). We refer the reader to Y15 for a detailed discussion of the consequences of such long time recoveries. However, we will reiterate here, that while both the spectral and temporal properties of SGR 1806–20 have now reached a quiescent state, it is clear that they did not follow the same long-term relaxation trend. The source X-ray flux started decaying immediately following the peak of the 2004 outburst (Y15, Figure 5), while the temporal properties lingered at a large historical level between 2005 and 2011 when the source was still moderately bursting. It reached a historically low level in 2015, following 6 years of a burst-quiet period. This reinforces our Y15 conclusion that low-level seismic activity causing small twists in the open field lines might be driving

torque variations without having any noticeable effects on the spectral behavior from the source.

The conspicuous result in the 0.5–10 keV flux recovery of SGR 1806–20 after the 2004 outburst is the lower quiescent level derived with *NuSTAR* compared with the long-term average pre-outburst, which persisted from 1993 to 2003 (Figure 5). The ratio of the 0.5–10 keV *NuSTAR* flux to the historical average flux is  $0.53 \pm 0.10$ , i.e., a factor of  $\sim 2$  smaller. A similar behavior was noticed in the flux evolution of SGR 1900+14: the source flux prior to the 1998 GF as measured over a 2-year period was at the  $1 \times 10^{-11} \text{ erg s}^{-1} \text{ cm}^{-2}$  level (Woods et al. 2001), while the flux in 2005, after almost 3 years during which no bursts were detected, reached half that value, i.e.,  $0.5 \times 10^{-11} \text{ erg s}^{-1} \text{ cm}^{-2}$  (Mereghetti et al. 2006), another example of a factor of 2 change in the recovery to the apparent quiescent state.

These lower asymptotic fluxes relative to their respective historical level constitute an interesting result. It is possible that this might potentially be due to a reconfiguration of the internal magnetic field in association with the lead up to the GF. Changes in crustal field morphology could affect the heat conduction between the hot neutron star core and the surface; such a conductivity is extremely efficient in polar zones where the magnetic field lines are oriented approximately vertically. One might then expect heating of the surface and also energy deposited in the magnetosphere approximately contemporaneous with adjustments to field structure. This might explain the rising quiescent BB+PL fluxes during the main bursting episode prior to the GF. The subsequent flux decline would signal an ensuing cooling phase. A possible signature of a permanent reconfiguration could be an alteration of the effective area of the BB component. Unfortunately, the uncertainty in the BB flux determination from *NuSTAR* spectroscopy precludes clear inferences of this possibility (see Table 2), though there is a slight hint of a net area reduction over the 15-year period.

#### 4.3. Spectral Models

The non-thermal spectra obtained in our *NuSTAR* observations of SGR 1806–20, embodied in Figure 4, are quite similar to the hard X-ray tail components in other magnetars (e.g., see Götz et al. 2006; Enoto et al. 2010, 2017; Vogel et al. 2014; Tendulkar et al. 2015; Younes et al. 2017). Yet, the power-law fit index of  $\Gamma = 1.33 \pm 0.03$  we obtain is slightly flatter than the typical values obtained in other observations of this source. Mereghetti et al. (2005) derived  $\Gamma = 1.5 \pm 0.3$  from 2004 *INTEGRAL*-IBIS observations just prior to the GF in December of that year. (Esposito et al. 2007) obtained  $\Gamma = 2.0 \pm 0.2$  from *Suzaku* HXD-PIN data from September 2006 in the 10–40 keV range, while (Enoto et al. 2010) determined  $\Gamma = 1.7 \pm 0.1$  with 2007 data from *Suzaku*. A more recent summary of *Suzaku* observations for SGR 1806-20 and other magnetars is presented in Enoto et al. (2017). Thus, while there was at first a suggestion of spectral flattening associated with the lead up to the GF, the fits obtained here indicate that there appears to be no clear evolutionary trend of the power-law index during the recovery phase following that extreme outburst.

The most popular paradigm for the generation of the hard X-ray components in magnetars is resonant inverse Compton scattering (Baring & Harding 2007; Fernández & Thompson 2007). Relativistic electrons, accelerated in the inner magnetosphere in closed field line regions with highly super-Goldreich

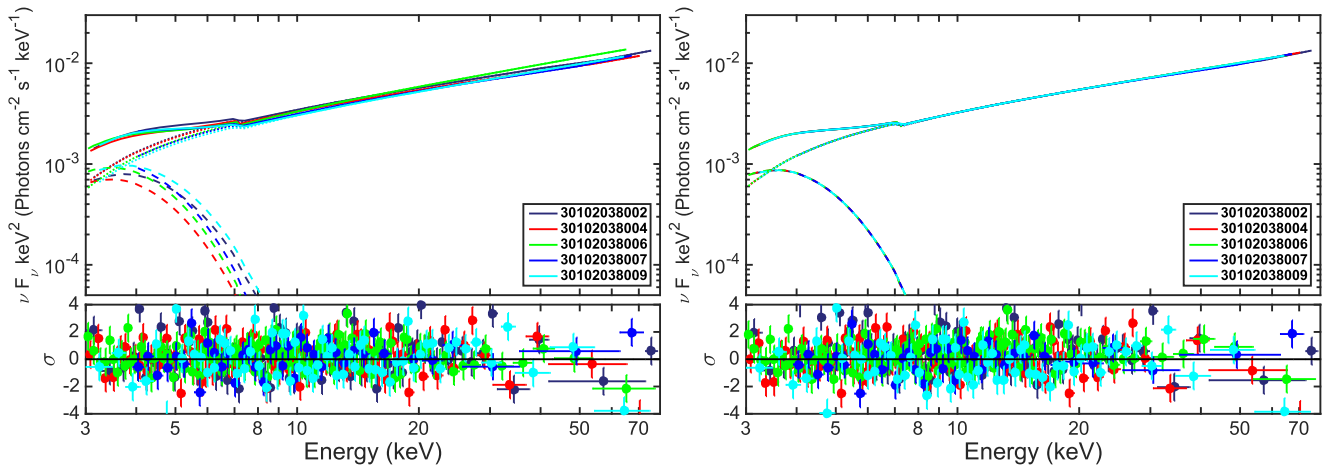


**Figure 4.** BB+PL best-fit model to all *NuSTAR* observations shown in  $\nu F_\nu$  space. Left panels: parameters are left free to vary between all observations, except for the absorption column density. Right panels: all parameters linked between the five observations to provide an ensemble average determination for them. The upper panels show the unfolded BB (dashed lines) and PL (solid lines) components. Data points were removed for clarity. The lower panels show the residuals in terms of the standard deviation  $\sigma$ .

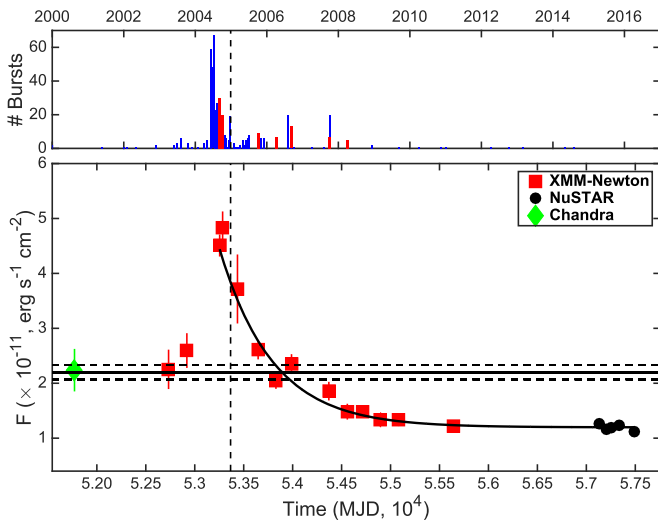


**Figure 5.** Total, absorption-corrected 0.5–10 keV flux evolution of SGR 1806–20 since 2000. The solid line is an exponential decay fit to the data from the time of the first *XMM-Newton* observation post-outburst, MJD 53254 (2004 September 6), to the last *NuSTAR* observation, MJD 57490 (2016 April 12). The characteristic decay timescale is  $\tau = 543 \pm 75$  days. Again, the dashed vertical line marks the date of the giant flare, MJD 53366 (2004 December 27). The horizontal solid line marks the historical flux level between 1993 and 2001, with the parallel dashed lines defining the  $1\sigma$  deviation. See the text for details. Color coding for the bars and points is as in Figure 3.

Julian densities, upscatter the abundant soft X-ray photons emanating from magnetar atmospheres. This process is extremely efficient, as the scattering is resonant at the cyclotron energy (e.g., Herold 1979), enhanced by over two orders of magnitude relative to the Thomson value. This can thereby effectively convert electron kinetic energy into radiative form (Baring et al. 2011). The kinematics of this process make for the generation of flat spectra if the electrons are mono-energetic (Baring & Harding 2007), with quasi-power-law indices of  $\Gamma \sim 0$  that are of lower value in general than those for the typical hard X-ray observations. In the magnetic Thomson construction of Beloborodov (2013), integrating over emission volumes and limiting the maximum Lorentz factor  $\gamma_e$  of the electrons can generate emission spectra that approximate

magnetar hard X-ray components quite well, as is demonstrated by the detailed comparison of models with spectral data for three magnetars in (Hascoët et al. 2014, see also, An et al. 2013, 2015; Vogel et al. 2014).

Yet there is great complexity in full QED analyses of resonant Compton upscattering spectra, as expounded in Wadiasingh et al. (2017) for mono-energetic electrons. Therein, flat spectra from resonant scatterings involving electrons moving along individual field lines, are steepened when integrating over toroidal surfaces. Moreover, there is the expectation that integrations over volumes within about 10 stellar radii of the surface, and the introduction of electron cooling, will soften these further to be approximately commensurate with the  $\Gamma$  values presented for SGR 1806–20 here. Depending on the observer viewing perspective, and the electron Lorentz factor, the quasi-power laws can extend down into the soft X-rays below 3 keV. Generally, this contribution is obscured by the thermal atmosphere component. However, SGR 1806–20 presents a special case in that the power-law tail component blends closely into the thermal (BB) portion of the spectrum, as is evident in Figure 4, which closely resembles the BB+PL combination in Figure 1 of Enoto et al. (2010). This property of an unusually high luminosity for the PL component (more so than for other magnetars; see Götz et al. 2006; Enoto et al. 2010) provides a significant constraint on resonant upscattering models that is yet to be fully explored. It affords the prospect of probes of the emission geometry and the values of the relativistic electron Lorentz factors and number density.

So too does the pulse profile information in Figure 2, which in one particular epoch evinces a double-peaked profile. Wadiasingh et al. (2017) illustrate how such double peaks can arise when the viewing angle  $\zeta$  and the magnetic axis angle  $\alpha$  to the rotation axis  $\Omega$  are similar in value, specifically for emission from toroidal field surfaces. In such cases, the line of sight can sweep across quasi-polar regions as the star rotates. This temporal feature diminishes when the emission volume expands to encapsulate a range of field line maximum altitudes and resonant interaction locales, and the phase separation of the two peaks (see Figure 12 of Wadiasingh et al. 2017) declines with increasing photon energy. Thus, as is the circumstance for gamma-ray pulsars, such pulse profiles provide an important

probe of the magnetic inclination  $\alpha$  of a magnetar, a prospect that is addressed in the *NuSTAR* analysis of data between 20 and 35 keV from 1E 1841-045 (An et al. 2013, 2015). More model development is needed to interpret these properties with greater precision, and the observations we present here set the scene to motivate such theoretical analyses. We anticipate that our results for SGR 1806–20 here can help inform the understanding of magnetar emission geometry, and the activation (and its evolution) of the magnetosphere in the decades subsequent to GF events.

This work made use of data from the *NuSTAR* mission, a project led by the California Institute of Technology, managed by the Jet Propulsion Laboratory and funded by NASA. We thank the *NuSTAR* Operations, Software, and Calibration teams for support with the execution and analysis of these observations. This research has made use of the *NuSTAR* Data Analysis Software (NuSTARDAS) jointly developed by the ASI Science Data Center (ASDC, Italy) and the California Institute of Technology (USA). G.Y. acknowledges support from NASA under *NuSTAR* Guest Observer cycle-1 program 01166, proposal number 14-NuSTAR14-0030. M.G.B. acknowledges the generous support of the NASA Astrophysics Theory Program through grant NNX13AQ82. V.M.K. receives support from an NSERC Discovery Grant, an Accelerator Supplement and from the Gerhard Herzberg Award, an R. Howard Webster Foundation Fellowship from the Canadian Institute for Advanced Research, the Canada Research Chairs Program, and the Lorne Trottier Chair in Astrophysics and Cosmology. J.G. acknowledges support from the Israeli Science Foundation under grant No. 719/14.

### ORCID iDs

George Younes  <https://orcid.org/0000-0002-7991-028X>  
 Chrysta Kouveliotou  <https://orcid.org/0000-0003-1443-593X>  
 Alice Harding  <https://orcid.org/0000-0001-6119-859X>  
 Ersin Göğüş  <https://orcid.org/0000-0002-5274-6790>  
 Victoria Kaspi  <https://orcid.org/0000-0001-9345-0307>  
 Jonathan Granot  <https://orcid.org/0000-0001-8530-8941>

### References

Alford, J. A. J., & Halpern, J. P. 2016, *ApJ*, 818, 122  
 An, H., Archibald, R. F., Hascoët, R., et al. 2015, *ApJ*, 807, 93  
 An, H., Hascoët, R., Kaspi, V. M., et al. 2013, *ApJ*, 779, 163  
 Archibald, R. F., Kaspi, V. M., Ng, C.-Y., et al. 2015, *ApJ*, 800, 33  
 Arnaud, K. A. 1996, in ASP Conf. Ser. 101, *Astronomical Data Analysis Software and Systems V* (San Francisco, CA: ASP), 17  
 Baring, M. G., & Harding, A. K. 2007, *Ap&SS*, 308, 109  
 Baring, M. G., Wadiasingh, Z., & Gonthier, P. L. 2011, *ApJ*, 733, 61  
 Beloborodov, A. M. 2013, *ApJ*, 762, 13  
 Beloborodov, A. M., & Thompson, C. 2007, *ApJ*, 657, 967  
 Bernardini, F., Israel, G. L., Dall’Osso, S., et al. 2009, *A&A*, 498, 195

Bibby, J. L., Crowther, P. A., Furness, J. P., & Clark, J. S. 2008, *MNRAS*, 386, L23  
 Bildsten, L., Chakrabarty, D., Chiu, J., et al. 1997, *ApJS*, 113, 367  
 Camilo, F., Ransom, S. M., Halpern, J. P., et al. 2016, *ApJ*, 820, 110  
 Chen, A. Y., & Beloborodov, A. M. 2017, *ApJ*, 844, 133  
 Coti Zelati, F., Rea, N., Turolla, R., et al. 2017, *MNRAS*, 471, 1819  
 Davis, J. E. 2001, *ApJ*, 562, 575  
 Dib, R., & Kaspi, V. M. 2014, *ApJ*, 784, 37  
 Enoto, T., Nakazawa, K., Makishima, K., et al. 2010, *ApJL*, 722, L162  
 Enoto, T., Shibata, S., Kitaguchi, T., et al. 2017, *ApJS*, 231, 8  
 Esposito, P., Mereghetti, S., Tiengo, A., et al. 2007, *A&A*, 476, 321  
 Fernández, R., & Thompson, C. 2007, *ApJ*, 660, 615  
 Gaensler, B. M., Kouveliotou, C., Gelfand, J. D., et al. 2005, *Natur*, 434, 1104  
 Gavriil, F. P., Kaspi, V. M., & Woods, P. M. 2004, *ApJ*, 607, 959  
 Götz, D., Mereghetti, S., Tiengo, A., & Esposito, P. 2006, *A&A*, 449, L31  
 Göğüş, E., Lin, L., Roberts, O. J., et al. 2017, *ApJ*, 835, 68  
 Granot, J., Gill, R., Younes, G., et al. 2017, *MNRAS*, 464, 4895  
 Halpern, J. P., & Gotthelf, E. V. 2005, *ApJ*, 618, 874  
 Harding, A. K., Contopoulos, I., & Kazanas, D. 1999, *ApJL*, 525, L125  
 Harrison, F. A., Craig, W. W., Christensen, F. E., et al. 2013, *ApJ*, 770, 103  
 Hascoët, R., Beloborodov, A. M., & den Hartog, P. R. 2014, *ApJL*, 786, L1  
 Herold, H. 1979, *PhRvD*, 19, 2868  
 Hurley, K., Boggs, S. E., Smith, D. M., et al. 2005, *Natur*, 434, 1098  
 Ibrahim, A. I., Markwardt, C. B., Swank, J. H., et al. 2004, *ApJL*, 609, L21  
 Israel, G. L., Romano, P., Mangano, V., et al. 2008, *ApJ*, 685, 1114  
 Kaplan, D. L., Fox, D. W., Kulkarni, S. R., et al. 2002, *ApJ*, 564, 935  
 Kargaltsev, O., Kouveliotou, C., Pavlov, G. G., et al. 2012, *ApJ*, 748, 26  
 Kaspi, V. M., Archibald, R. F., Bhalariao, V., et al. 2014, *ApJ*, 786, 84  
 Kaspi, V. M., & Beloborodov, A. 2017, *ARA&A*, 55, 261  
 Kennea, J. A., Burrows, D. N., Kouveliotou, C., et al. 2013, *ApJL*, 770, L24  
 Lin, L., Kouveliotou, C., Göğüş, E., et al. 2011, *ApJL*, 740, L16  
 Mereghetti, S. 2008, *A&ARv*, 15, 225  
 Mereghetti, S., Esposito, P., Tiengo, A., et al. 2006, *ApJ*, 653, 1423  
 Mereghetti, S., Tiengo, A., Esposito, P., et al. 2005, *ApJ*, 628, 938  
 Mori, K., Gotthelf, E. V., Zhang, S., et al. 2013, *ApJL*, 770, L23  
 Parfrey, K., Beloborodov, A. M., & Hui, L. 2013, *ApJ*, 774, 92  
 Pintore, F., Bernardini, F., Mereghetti, S., et al. 2016, *MNRAS*, 458, 2088  
 Rea, N., & Esposito, P. 2011, in *High-Energy Emission from Pulsars and their Systems*, ed. D. F. Torres & N. Rea (Berlin: Springer), 247  
 Rea, N., Tiengo, A., Mereghetti, S., et al. 2005, *ApJL*, 627, L133  
 Scholz, P., Kaspi, V. M., & Cumming, A. 2014, *ApJ*, 786, 62  
 Scholz, P., Ng, C.-Y., Livingstone, M. A., et al. 2012, *ApJ*, 761, 66  
 Tendulkar, S. P., Hascoët, R., Yang, C., et al. 2015, *ApJ*, 808, 32  
 Thompson, C., Lyutikov, M., & Kulkarni, S. R. 2002, *ApJ*, 574, 332  
 Tiengo, A., Esposito, P., Mereghetti, S., et al. 2005, *A&A*, 440, L63  
 Tong, H., Xu, R. X., Song, L. M., & Qiao, G. J. 2013, *ApJ*, 768, 144  
 Turolla, R., Zane, S., & Watts, A. L. 2015, *RPPh*, 78, 116901  
 van der Horst, A. J., Kouveliotou, C., Gorgone, N. M., et al. 2012, *ApJ*, 749, 122  
 Verner, D. A., Ferland, G. J., Korista, K. T., & Yakovlev, D. G. 1996, *ApJ*, 465, 487  
 Vogel, J. K., Hascoët, R., Kaspi, V. M., et al. 2014, *ApJ*, 789, 75  
 Wadiasingh, Z. 2017, *ApJ*, submitted  
 Wilms, J., Allen, A., & McCray, R. 2000, *ApJ*, 542, 914  
 Woods, P. M., Kouveliotou, C., Finger, M. H., et al. 2000, *ApJL*, 535, L55  
 Woods, P. M., Kouveliotou, C., Finger, M. H., et al. 2007, *ApJ*, 654, 470  
 Woods, P. M., Kouveliotou, C., Göğüş, E., et al. 2001, *ApJ*, 552, 748  
 Woods, P. M., Kouveliotou, C., Göğüş, E., et al. 2002, *ApJ*, 576, 381  
 Woods, P. M., Kouveliotou, C., van Paradijs, J., et al. 1999, *ApJL*, 524, L55  
 Younes, G., Kouveliotou, C., Grefenstette, B. W., et al. 2015a, *ApJ*, 804, 43  
 Younes, G., Kouveliotou, C., Jaodand, A., et al. 2017, *ApJ*, 847, 85  
 Younes, G., Kouveliotou, C., Kargaltsev, O., et al. 2012, *ApJ*, 757, 39  
 Younes, G., Kouveliotou, C., Kargaltsev, O., et al. 2016, *ApJ*, 824, 138  
 Younes, G., Kouveliotou, C., & Kaspi, V. M. 2015b, *ApJ*, 809, 165